

Settled fast measurement of topological charge by direct extraction of plane wave from vortex beam

Xiao-Bo Yang(杨晓波) and Jin Hu(胡进)

Citation: Chin. Phys. B, 2021, 30 (**10**): 104203. DOI: 10.1088/1674-1056/abec32
Journal homepage: http://cpb.iphy.ac.cn; http://iopscience.iop.org/cpb

What follows is a list of articles you may be interested in

Efficient manipulation of terahertz waves by multi-bit coding metasurfaces and further applications of such metasurfaces

Yunping Qi(祁云平) Baohe Zhang(张宝和), Jinghui Ding(丁京徽), Ting Zhang(张婷), Xiangxian Wang(王向贤), and Zao Yi(易早)
Chin. Phys. B, 2021, 30 (**2**): 024211. DOI: 10.1088/1674-1056/abd6fc

Propagation properties and radiation force of circular Airy Gaussian vortex beams in strongly nonlocal nonlinear medium

Xinyu Liu(刘欣宇), Chao Sun(孙超), and Dongmei Deng(邓冬梅)
Chin. Phys. B, 2021, 30 (**2**): 024202. DOI: 10.1088/1674-1056/abcf3b

Visible-light all-fiber vortex lasers based on mode selective couplers

Chuchu Dong(董楚楚), Jinhai Zou(邹金海), Hongjian Wang(王鸿健), Han Yao(尧涵), Xianglong Zeng(曾祥龙), Yikun Bu(卜轶坤), Zhengqian Luo(罗正钱)
Chin. Phys. B, 2020, 29 (**9**): 094204. DOI: 10.1088/1674-1056/aba278

Properties of off-axis hollow Gaussian-Schell model vortex beam propagating in turbulent atmosphere

Yan-Song Song(宋延嵩), Ke-Yan Dong(董科研), Shuai Chang(常帅), Yan Dong(董岩), Lei Zhang(张雷)
Chin. Phys. B, 2020, 29 (**6**): 064213. DOI: 10.1088/1674-1056/ab836c

Propagation properties of radially polarized Pearcey-Gauss vortex beams in free space

Xinpeng Chen(陈鑫鹏), Chuangjie Xu(许创杰), Qian Yang(杨芊), Zhiming Luo(罗智明), Xixian Li(李希贤), Dongmei Deng(邓冬梅)
Chin. Phys. B, 2020, 29 (**6**): 064202. DOI: 10.1088/1674-1056/ab8202

Settled fast measurement of topological charge by direct extraction of plane wave from vortex beam*

Xiao-Bo Yang(杨晓波)[1,2,3] and Jin Hu(胡进)[1,3,†]

[1] School of Information and Electronics, Beijing Institute of Technology, Beijing 100081, China
[2] Institute of Information Engineering, Chinese Academy of Sciences, Beijing 100195, China
[3] China Beijing Key Laboratory of Fractional Signals and Systems, Beijing 100081, China

(Received 4 January 2021; revised manuscript received 24 February 2021; accepted manuscript online 5 March 2021)

A method of measuring the vortex beam topological charge (TC) is proposed based on a device that can directly extract the plane wave form from the vortex beam in which the different propagation angles of the plane waves are uniquely related to the different TCs. Then the TC can be obtained by simply comparing the energy values perceived by two fixed sensors in the detection location with the help of twin omnidirectional energy absorbers (OEAs). Because the settled detection relies only on the simple quantitative value at two fixed positions, neither pattern recognition nor field analysis procedure is applied, thus allowing faster measurement. Some features of the methodology are investigated, and the numerical simulations verify the feasibility and robustness of the system.

Keywords: vortex beam, topological charge, settled measurement

PACS: 42.25.–p, 42.30.Kq, 41.20.Jb **DOI:** 10.1088/1674-1056/abec32

1. Introduction

Vortex waves with orbital angular momentum (OAM)[1] have attracted considerable attention due to their unique beam characteristic of a continuous spiral phase $\exp(\mathrm{i}l\theta)$, where l is the topological charge (TC), and θ is the azimuthal angle. The special properties of such optical vortices possess widespread applications, such as in optical manipulation,[2] optical tweezers,[3] quantum information processing and cryptography,[4–6] free-space information transfer and communications,[7–9] super-resolution imaging,[10] astronomical coronagraphy,[11] and detection of rotating objects.[12–14] Accordingly, the determining of the OAM states, usually characterized by the TC, is important in several OAM applications. For example, in wireless communication that uses electromagnetic vortex technology, the multichannel information is encoded into multiple OAM states for transmission due to the orthogonality of different OAM states. The effective demodulation of the OAM states is a crucial issue in such a multiplexing system.

Several methods of TC detection and recognition have been reported. These were developed basically along two routes from the signal processing perspective, that is, by detection in the spatial domain and in the frequency domain or Fourier spectrum. Direct detection of the TC in the spatial domain is difficult due to requiring some manipulation of the beam, such as interference or diffraction correlation, to generate different wave field patterns according to different TCs. The vortex wave can easily interfere with the plane wave, spherical wave, or conjugate light wave.[15,16] Moreover, the diffraction or interference intensity modes can be obtained by using various diffractive apertures,[17–21] slits, or pinholes.[22–28] Recently, the multipoint interferometer (IMI) for measuring the OAM of an optical vortex with high topological charge[29] and digital micromirror device for probing the OAM of Laguerre–Gaussian (LG) beams[30] were also proposed. Some special gratings have been used to produce miscellaneous diffraction patterns.[31–34] Other devices or technologies, such as specific prisms or phase plates,[35–42] have also been investigated.

Regarding detection in the frequency domain, the key idea is to accomplish the Fourier transform (FT) of the input vortices. With the help of optical geometric transformation, the OAM states can be observed in the Fourier spectrum, in which the vortex beam is translated into plane wave before the FT.[43] The lateral and tilt misalignment information of the input beam can be reformatted, and the OAM spectrum after the FT can be measured.[44] In addition, a special transformation that maps spirals into parallel lines can be used to obtain a plane wave for the FT, which results in a high-resolution OAM mode.[45] The intensity distribution of the FT can be combined with the orthogonality of the Laguerre polynomials to detect the TC.[46] The coordinate transformation method can be used to obtain the diffraction field distribution for the FT to identify the fractional TC.[47] In addition, an axicon,[48] tilted spherical lens,[49] and circular plasmonic lens[50] were proposed to be used to obtain the spatial spectrum of the intensity pattern

*Project supported by the National Natural Science Foundation of China (Grant Nos. 61975015, 61575022, and 61421001) and the Beijing Natural Science Foundation, China (Grant No. L191004).

†Corresponding author. E-mail: bithj@bit.edu.cn

© 2021 Chinese Physical Society and IOP Publishing Ltd

in measuring the TC.

These technologies, whether the detection is carried out in the spatial domain or in the spectrum domain, are based on the analysis of the wave field distribution in a region and require the varying distribution patterns to be identified to obtain different TC information, such as counting the stripe numbers, categorizing the vein sharps, and sorting the peak positions. This task may consume more resources and presents a challenge to real-time detection. In view of this, some methods or devices with low requirements for calculation or analysis in wave field measurement were proposed. For example, the method of measuring the real-time phase of optical vortices has been achieved based on the pixel micro polarizer array (PMA), where the acquisition of phase only needs to pass through one frame image;[51] the plasmonic photodiode device based on holographic method can selectively detect the orbital angular momentum of light;[52] the silicon integrated OAM detector based on the microscale waveguide can detect the OAM of the vortex beam in real time.[53] These systems, though they have less or simpler valuation processes, are still limited by the step of wave field analysis and usually need complex configurations.

In the present work, a new TC measurement method without the pattern recognition procedure is proposed, in which the TC is measured by detecting the values of the wave energy at two fixed positions. The method of TC detection based on a few fixed positions is called settled detection or measurement to distinguish it from techniques based on field pattern recognition or wave field analysis. This method offers a fast and easy way to measure the vortex beam TC and can have potentially wide applications in relevant fields. The rest of the report is organized as follows: Section 2 presents the design of the proposed device and the analyses of its properties. Section 3 performs the numerical simulations to verify the device performance. The discussion and conclusions are presented in Section 4.

2. Design of settled detection device

In general, the complex amplitude of a canonical optical vortices can be expressed as

$$U(x,y,z) = A\exp(\mathrm{i}l\theta(x,y)), \tag{1}$$

where A and θ are the amplitude and the azimuthal angle ranging from 0 to 2π, l is the TC and an integer in a range between $-\infty$ and ∞, which determines the number of 2π phase shifts that occur across one revolution of θ. The azimuthal angle can be written in Cartesian coordinates as

$$\theta(x,y) = \arctan\left(\frac{y}{x}\right) = \arctan(\tau), \tag{2}$$

If $|\tau| = |y/x| \leq 1$ or $|\theta| \leq \pi/2$, the Taylor expansion of $\arctan(\tau)$ is as follows:[54]

$$\arctan(\tau) = \sum_{v=0}^{\infty} \frac{(-1)^v}{2v+1}\tau^{2v+1}, \tag{3}$$

where if $|\tau|$ is sufficiently small, the high order term in the Taylor expansion can be ignored, thereby resulting in

$$\theta = \arctan(\tau) \cong \tau = \frac{y}{x}. \tag{4}$$

Then

$$\exp(\mathrm{i}l\theta) = \exp(\mathrm{i}l\tau) = \exp\left(\mathrm{i}l\frac{y}{x_0}\right), \tag{5}$$

where x_0 is a constant, and $|y|$ is far less than $|x_0|$, which means that the spiral wave front $f = \exp(\mathrm{i}l\theta)$ is transformed into a tilted plane wave front $f' = \exp(\mathrm{i}ly/x_0)$ at location $x = x_0$. Under this condition, the OAM modes with different TC values are transformed into a plane wave with a different propagation angle, which can be further detected and processed more easily.

Figure 1 presents such a spiral-to-plane transfer system without loss of generality. Take a thin layer, here in this study called a detection layer, to be parallel to the optical (z) axis, and set such an input aperture on the layer that it satisfies the previous approximation condition, that is, x is a fixed value $|x_0|$, and the aperture width is far less than $|x_0|$. To guide sufficient wave into the detection layer, the wavelength should be small enough compared with the size of the input aperture.

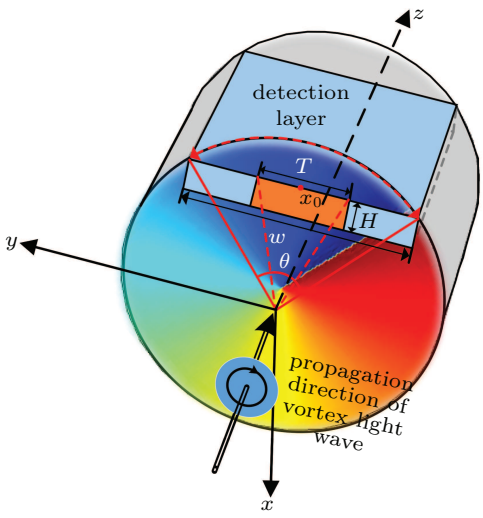


Fig. 1. Structural diagram of spiral-to-plane transfer system, where x_0 is fixed in value aperture width $T \leq |x_0|$, and detection layer thickness H is small enough.

To further clarify the relation between the vortex beam TC and the plane wave propagation direction, the phase term is rewritten as

$$\exp(\mathrm{i}ly/x_0) = \exp(\mathrm{i}ky\cos(\beta)), \tag{6}$$

where $k = 2\pi/\lambda$ is the wave number, $\cos(\beta)$ is the direction cosine along the y direction, and λ is the wavelength: it is easy to obtain from

$$l = \frac{2\pi x_0}{\lambda}\cos(\beta). \tag{7}$$

The vortex beam TC is found to be directly proportional to the direction cosine of the plane wave, and the different propagation directions lead to different wave distributions in the detection place. Thus, the TC can be obtained from these differences. The different energy proportions perceived by some fixed sensors in the detection location are proposed to be used to characterize and identify the wave distributions based on a simple quantitative value without pattern recognition. In particular, to avoid using a sensor array or vast sensors, two omnidirectional energy absorbers (OEAs)[55] can be symmetrically blocked on the wave propagation path in the detection layer to guide the whole propagating wave into the absorption cores. The waves in the detection layer are supposed to be attracted into the twin absorption positions, and the different propagation directions, which correspond to different TCs, can be determined by the different energy proportions perceived by the two sensors fixed respectively at the two absorption cores.

The optical OEA[55] consists of a shell that controls the ray trajectory and a core that absorbs the wave energy. The refractive index of the OEA is

$$n = \begin{cases} n_0\left(\dfrac{R}{r}\right)^m, & R_c < r < R, \\ n_0, & r \geq R, \end{cases} \tag{8}$$

where r is the radial coordinate of the OEA, R is the outer radius of the OEA, R_c is the absorption core radius, and n_0 is the refractive index of the background (detection layer). From the transformation perspective, the function of this device is equivalent to mapping the wave field at infinity to the central position[56] to enable it to absorb all the wave fields that enter into both the outer boundary and the inner absorption core. A larger value of m implies that the system is more attractive and that an incident beam will fall more rapidly into the core, whereas $m = 2$ denotes a critical condition in which the beam can be captured. To mimic the enough layer width, the domain boundary condition can be set to be the scattering boundary condition (SBC) to avoid the reflection. The core $(r < R_c)$ has a sensor for collecting the electromagnetic energy. Figure 2 shows the settled detection device diagram based on twin OEAs. Figure 2(a) is the whole configuration (for details, see Fig. 1) and figure 2(b) is a top view of the detection layer in Fig. 2(a) where the two blue ring areas are OEA devices with sensors fixed at their cores, respectively.

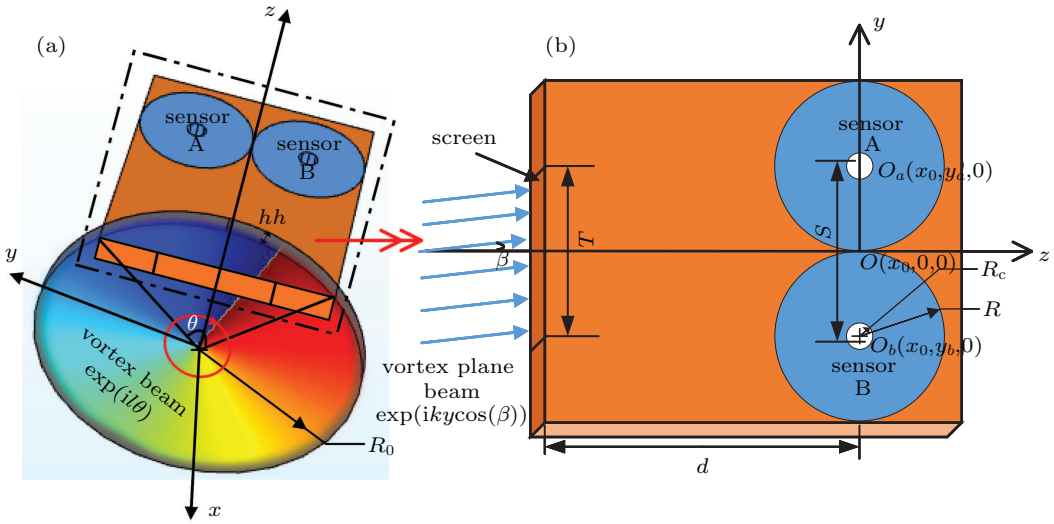


Fig. 2. Diagram of settled detection device based on twin OEAs: showing (a) the whole structure of the device and (b) detailed structure of detection layer, where input aperture width is T and distance between sensors A and B is S.

The advantage of this method is that the TC can be obtained directly by quantitatively measuring the energy value of the wave field at the fixed position but not by recognizing the wave field distribution patterns, thus enabling fast measurement.

Further study of the relation between the TC and the energy proportion detected in the sensors is important. According to Huygens–Fresnel diffraction integral theory, the diffraction field distribution satisfies the Fresnel diffraction over a short transmission distance.[57] The Fresnel diffraction of the observation plane is expressed as

$$E(x_1,y_1,z) = -\frac{\mathrm{i}}{\lambda z}\exp(\mathrm{i}kz)\iint T_1(x,y)U(x,y,0) \times \exp\left\{\frac{\mathrm{i}k}{2z}[(x-x_1)^2+(y-y_1)^2]\right\}\mathrm{d}x\mathrm{d}y, \tag{9}$$

where the wave propagates along the z direction, and $U(x,y,0)$ is the input signal, $T_1(x,y)$ is a window function, and (x_1,y_1) is the coordinates of observation plane. The propagation di-

rection or direction cosine is related to the coordinates in input and observation planes, such as $\cos(\alpha) = (x - x_1)/z = 0, \cos(\beta) = (y - y_1)/z$. In two-dimensional (2D) space, such as in the y–z plane, the final Fresnel diffraction is reduced to

$$E(y_1, z) = -\frac{\mathrm{i}}{\lambda z}\exp(\mathrm{i}kz)\int T_1(y)U(y,0) \times \exp\left\{\frac{\mathrm{i}k}{2z}[z\cos(\beta)]^2\right\}\mathrm{d}y. \quad (10)$$

From the perspective of signal processing, the Fresnel diffraction of the optical field is equivalent to the fractional Fourier transform (FrFT) of the input signal. The order of the FrFT can be observed at a distance b from the screen. As b is increased from 0 to ∞, the order of the fractional transform increases from 0 to 1.[58,59] The order of the FrFT can be explained as the degree of a signal transform from its spatial domain to the frequency domain; thus, a small order or short propagation distance means that the signal is similar to its original profile. Figure 3 shows the detection principle. The wave field in the detection line can be divided into two parts by the central point C, denoted by p and q, respectively. The wave that propagates to the two areas enters into the twin OEAs, respectively. The length ratio between part p and part q approximately corresponds to the ratio between the values of wave energy in the two sections if the input wave field is uniform.

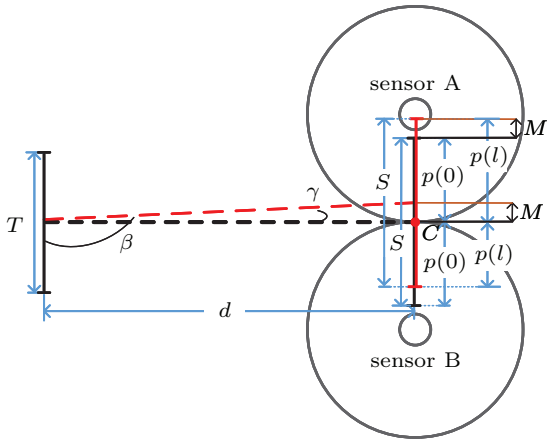


Fig. 3. Distribution structure of wave field absorbed by twin OEAs where $p(l)$ and $q(l)$ denote wave energy values absorbed into twin OEAs, respectively, with l being TC when $l \neq 0, p(l) \neq q(l)$.

From Eq. (7) it is obtained that

$$\beta = \arccos\left(\frac{l\lambda}{2\pi x_0}\right). \quad (11)$$

From Fig. 3, the offset distance of the wave field in the detection area caused by l is $M = d\tan(\gamma)$, where

$$\gamma = \left|\beta - \frac{\pi}{2}\right|. \quad (12)$$

Substituting Eq. (11) into Eq. (12), when γ or $l\lambda/2\pi x_0$ is small,

$$\tan(\gamma) \cong \gamma = \left|\arccos\left(\frac{l\lambda}{2\pi x_0}\right) - \frac{\pi}{2}\right| = \arcsin\left(\frac{l\lambda}{2\pi x_0}\right) \cong \frac{l\lambda}{2\pi x_0}. \quad (13)$$

Therefore, approximately, we have

$$M = d\tan(\gamma) = d\gamma = \frac{dl\lambda}{2\pi x_0}. \quad (14)$$

In this case, the ratio between p and q, *i.e.*, the energy ratio (ER) is

$$K = \frac{p(l)}{q(l)} = \frac{p(0)+M}{q(0)-M} = \left(1+\frac{d}{\pi x_0 S}l\lambda\right)\Big/\left(1-d/\pi x_0 S l\lambda\right), \quad (15)$$

where $p(0) = q(0) = S/2$ and S is the length of the detection line. The Taylor expansion of the above formula gives[60]

$$K = 1 + 2\left(\frac{d}{\pi x_0 S}\right)l\lambda + o\left(\frac{d}{\pi x_0 S}l\lambda\right)^2. \quad (16)$$

Ignoring the higher order terms,

$$K = 1 + \frac{2d}{\pi x_0 S}l\lambda. \quad (17)$$

This equation shows that the ER has an approximate linear relationship with the TC (l) and the wavelength (λ). Although the linear approximation cannot be established when the detection surface is far away, γ is large, or the input wave field is not uniform, a corresponding relation between the TC and the ER still exists, which can still be used to determine the TC, but the settled detection scheme will work in a more complicated way which is beyond the present discussion.

The structure of the system is simple, however some of its properties should be further investigated in order to optimize the performance in various circumstances. As shown in Fig. 3, the distance d from the sensors to the input aperture should be suitable for the application. If d is large, the offset distance M for the same input should be large, which means that the system has higher TC distinguishability according to Eq. (15). On the other hand, the long d will limit the maximal TC that can be detected. If M is too large (approaches to $S/2$), almost all wave fields will come into one OEA but no input energy enters into the other one, thus Eq. (15) does not hold any more. The input aperture width T also needs a balanced size. Small T satisfies the spiral-to-plane transfer condition Eq. (4) better, however, for the same reason the number of TCs the system can perceive will decrease. In addition, the system size should be larger enough than the wave length for normal propagation: small T will limit the working wave length. In our study, we choose the aperture width to be close to the OEA diameter and the simulation result shows that it has no significant difference from that with half the width. The OEA cannot be perfect in practice. Suppose that its absorption ratio is Ar ($0 < Ar < 1$), then an interesting and important conclusion will be that this imperfection will not influence the system if the two OEAs

are the same. This can be shown by multiplying both $p(l)$ and $q(l)$ by Ar in Eq. (15), and $K = p(l)Ar/[q(l)Ar] = p(l)/q(l)$ still holds true. Another interesting property of the system is that one detection layer uses only a fraction of the input facet, so it is possible to take advantage of the abundant space to achieve multiple detection layers for enhancing the detection robustness or efficiency.

3. Numerical simulations

3.1. Validity of proposed method

To verify the performance of the device, a numerical simulation based on COMSOL Multiphysics is carried out. Because the working principle depends only on the relative size of the device relative to the wavelength, the length unit is ignored here; this can be set to be mm or μm, for example, if need be. As shown in Fig. 2, the radius of the plane with the vortex beam input is $R_0 = 2.12$ and the input aperture width of the input plane is $T = 1.2$. The detection layer has length $L = 3$, width $W = 2.4$, height $H = 0.3$, and detection distance $d = 2$, and the detection layer is located at $x_0 = 1.5$ and refractive index $n_0 = 1$.

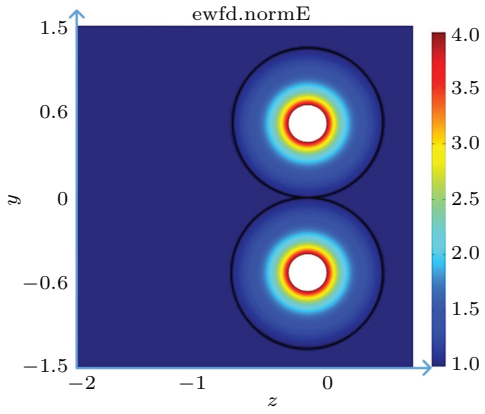


Fig. 4. Refractive index profile of detection layer with twin OEAs.

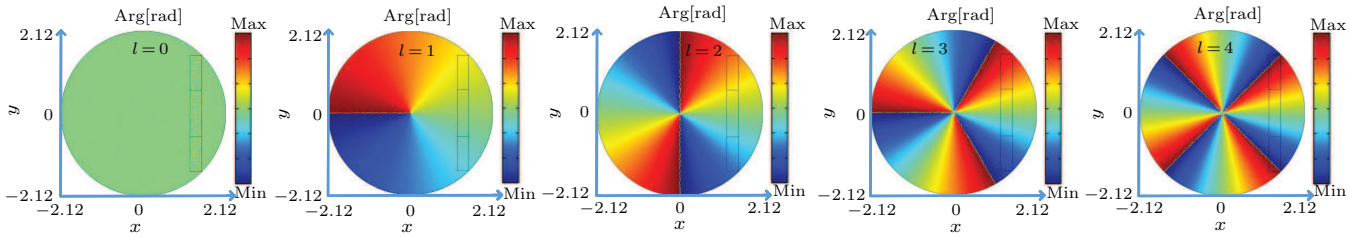


Fig. 5. Phase distributions of input vortex signals.

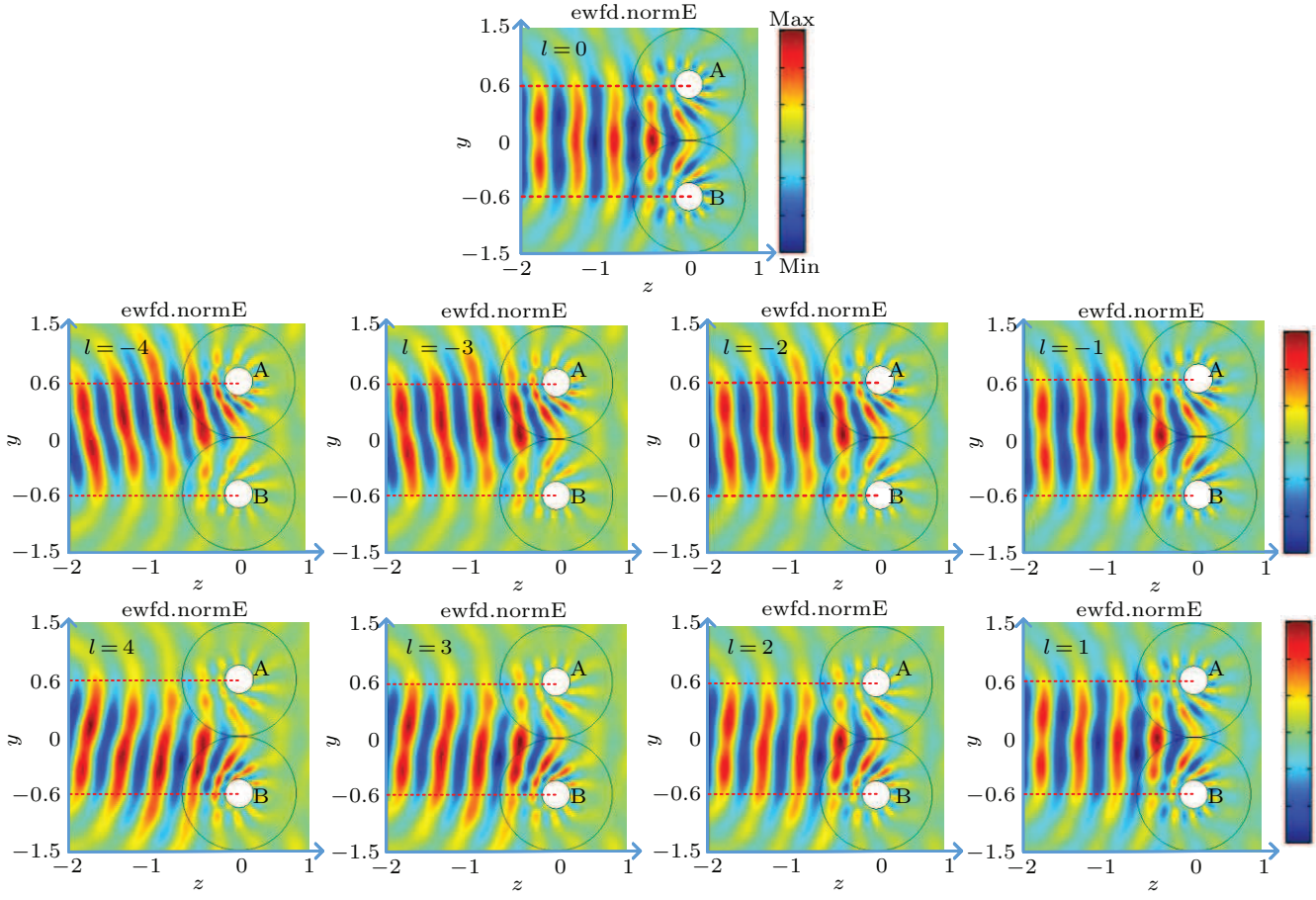


Fig. 6. Wave field distributions on top surface of detection layer.

The parameters of the twin OEAs are $R = 0.6$ and $R_c = 0.15$. The attractive parameter $m = 2$ is chosen in the twin OEAs because the lower refractive index gradient is more practical in engineering. Figure 4 shows the refractive index distribution of the detection layer. Figure 5 presents the phase distributions of the input vortex signals with the TC ranging from 0 to 4.

Because the detection layer is thin, the difference in energy between the top and bottom surfaces is not obvious. Thus, only the wave fields on the top surface are considered here in this work. Sensors A and B are located at the two absorption cores, respectively. Figure 6 shows the wave field distributions when the wavelength of the input electromagnetic wave is $\lambda = 0.4$. As shown in the figure, when $l = 0$, the input light wave is evenly absorbed into the sensors. When $l \neq 0$, the wave fields absorb different amounts of energy by sensors A and B according to the varying l. Therefore, the TC can be determined by the ratio between the wave energy values in the two sensors.

Table 1 shows the ratio between the high and low energy values in sensors A and B shown in Fig. 6 when the length unit is chosen as μm.

Table 1. Numerically calculated values of ER and TC.

TC	Energy in A (V/um)	Energy in B (V/um)	ER (large/small)
–4	68.26	34.82	1.96
–3	66.25	39.93	1.66
–2	63.47	45.87	1.38
–1	59.85	51.61	1.16
0	55.37	56.58	1.02
1	50.25	60.55	1.20
2	44.76	63.52	1.42
3	39.25	66.00	1.68
4	34.38	68.48	1.99

Figure 7 presents the data in Table 1, which shows that the ER has an approximate linear relation with the TC at a fixed wave length, which is in agreement with Eq. (17).

The wavelength can be additionally set to be $\lambda = 0.5$ and $\lambda = 0.6$ separately. Table 2 presents the ER corresponding to the TC ranging from 0 to 4 at different wavelengths; their fit curves are shown in Fig. 8. The results are also in agreement with Eq. (17).

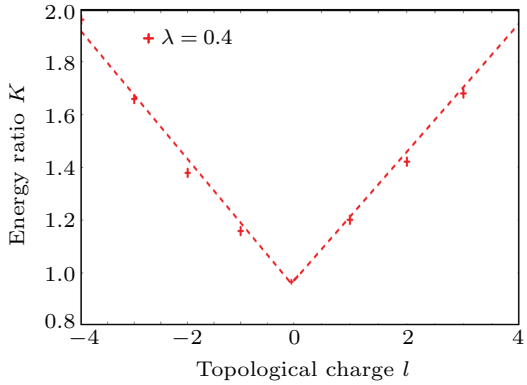


Fig. 7. Numerically calculated relation of ER with TC.

Table 2. Numerically calculated values of ER and TC at different wavelengths.

TC (l)	ER ($\lambda = 0.4$)	ER ($\lambda = 0.5$)	ER ($\lambda = 0.6$)
0	1.02	1.01	1.04
1	1.20	1.27	1.37
2	1.42	1.61	1.79
3	1.68	2.00	2.30
4	1.99	2.42	2.86

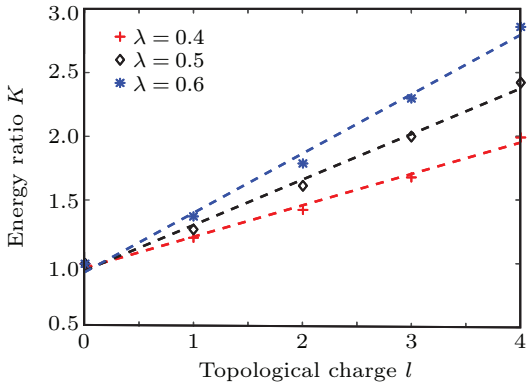


Fig. 8. Numerically calculated relation of ER with TC at different wavelengths.

To evaluate the accuracy of the proposed model, the theoretical and simulation values of the ER are compared with each other. The theoretical results are obtained from Eq. (17), whereas the field width S is approximately set to be the input aperture width T. Table 3 presents the comparison, indicating that the mathematical model is in accordance with the numerical simulation.

Table 3. Comparison between theoretical and simulation values of ER for different TCs.

TC (l)	ER ($\lambda = 0.4$)			ER ($\lambda = 0.5$)			ER ($\lambda = 0.6$)		
	TV	SV	RE	TV	SV	RE	TV	SV	RE
0	1.00	1.02	2%	1.00	1.01	1%	1.00	1.04	4%
1	1.30	1.20	7%	1.37	1.27	7%	1.45	1.37	5%
2	1.59	1.42	11%	1.74	1.61	8%	1.89	1.79	5%
3	1.89	1.68	11%	2.11	2.00	5%	2.34	2.30	2%
4	2.19	1.99	9%	2.49	2.42	3%	2.78	2.86	3%

Notes: TV: theoretical value; SV: simulation value; RE: relative error.

3.2. Robustness of proposed method

In practical applications, sometimes the beam or test environment is in a non-ideal situation, which may affect the performance of existing TC detection systems. For example, TC detection methods based on geometric transformation face problems such as crosstalk, inherent defects of beam transformation, and power loss. It is important to check the performance of the proposed method working in some imperfect conditions and the robustness examination may benefit the future applications. All the simulations here are carried out at a dimensionless wavelength of 0.4.

3.2.1. Beam incidence direction deviation

In an ideal situation, the vortex beam input is vertical to the detection device, or the propagation direction of the beam is strictly along the optical axis (z axis), so the input angle deviating from the optical axis is 0°. However, in practice, a small angle deviation may exist, so its influence degree of TC detection is discussed. Obviously, the influence depends on the incidence direction deviation that occurs in the x-axis direction or y-axis direction, and the general cases can be derived from these two special circumstances.

In the examination, the input deviations of 1°, 3°, and 5° are set to be along the x-axis direction and so are they along the y-axis direction The wave field distributions in the detection layer are shown in Fig. 9. The corresponding relation between the ER and the TC number is shown in Table 4, where the TC number is 0–4. The line diagram is presented in Fig. 10.

It can be seen from this demonstration that the system is much more sensitive to the input direction inclination along the y-axis direction than x-axis direction as expected, because the detection mechanism itself relies on the wave propagation direction in the y-axis direction. However, a tiny input angle error along the y-axis direction, *e.g.*, 1° in this simulation, can still be tolerated by the system. As the linear relation remains at different deviations, for those rougher systems, it is a good idea to make corresponding calibration before formal testing.

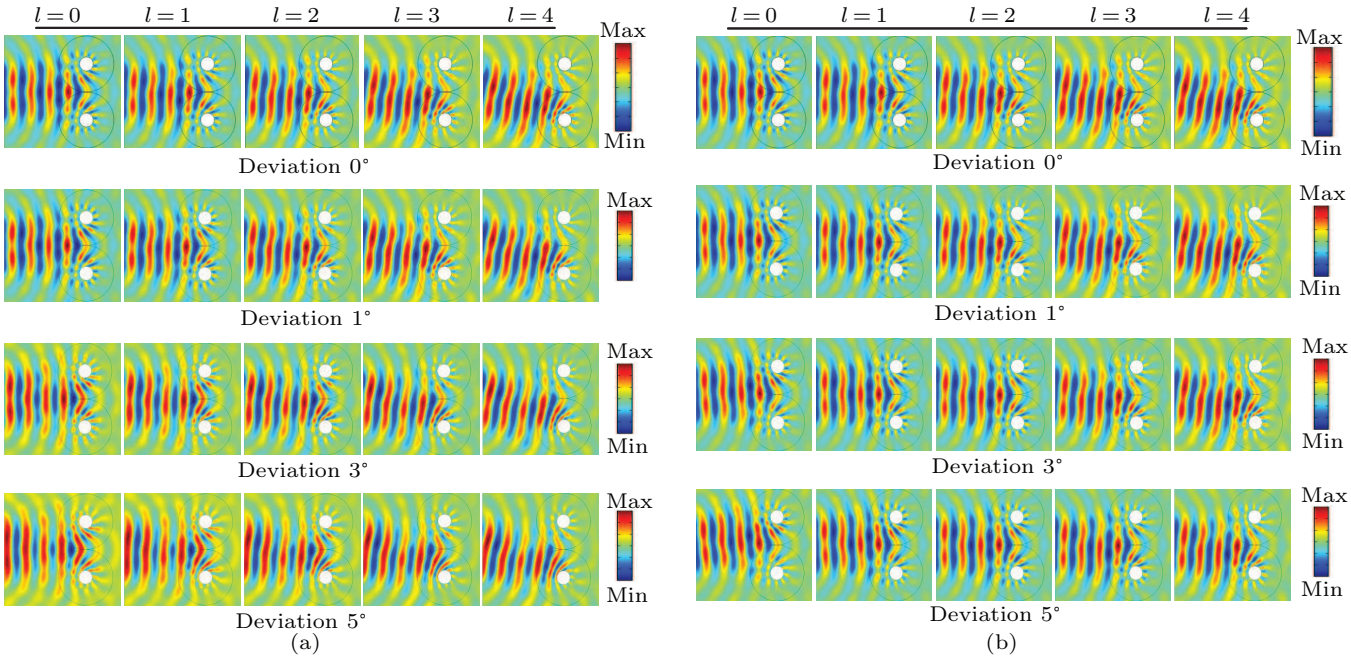


Fig. 9. Wave field distributions in detection layer when input angle deviations occur along (a) x-axis direction and (b) y-axis direction.

Table 4. Numerically calculated values of ER and TC of input vortex waves with different input angle deviations.

TC	ER (no deviation)	ER (nonideal) Input wave deviation in x direction			ER (nonideal) Input wave offset in y direction		
		Deviation 1°	Deviation 3°	Deviation 5°	Deviation 1°	Deviation 3°	Deviation 5°
0	1.02	1.02	1.02	1.02	0.95	0.81	0.69
1	1.20	1.21	1.21	1.22	1.12	0.96	0.82
2	1.42	1.43	1.44	1.46	1.32	1.13	0.97
3	1.68	1.70	1.72	1.75	1.56	1.33	1.15
4	1.99	2.02	2.06	2.11	1.85	1.58	1.36

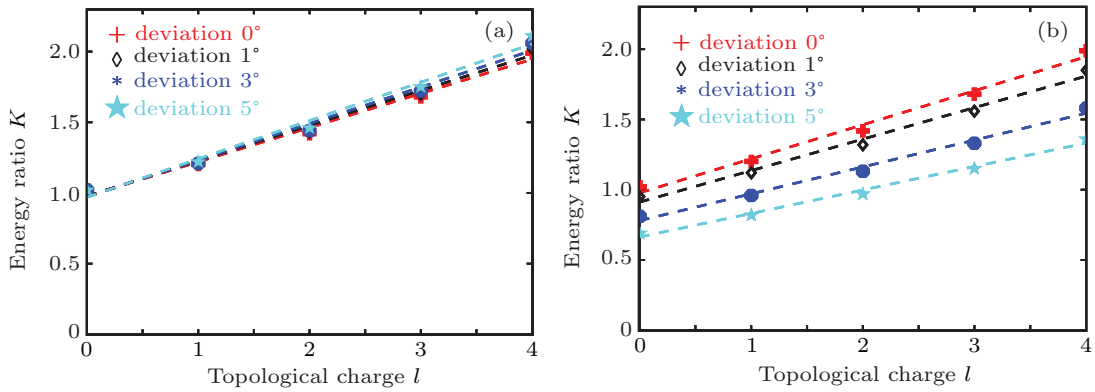


Fig. 10. Numerically calculated relation of ER with TC of input vortex light wave with certain deflection angles in (a) *x*-axis direction and (b) *y*-axis direction.

3.2.2. Input beam center offset

The ideal model requires the center of the beam to be exactly located at the center of the input disc (see Fig. 1). However, in practice, this condition may not be so perfectly satisfied and tiny position offset may exist. To evaluate the influence of such an error, here in the simulation the deviation distances of the input wave along the *x*-axis and *y*-axis directions are both set to be −0.2, −0.1, 0.1, and 0.2 dimensionless length, the wave fields can be found in Fig. 11 and the relation between the ER and the TC is shown in Table 5. Here, the TC is in a range of 0–4, and the linear relation is shown in Fig. 12.

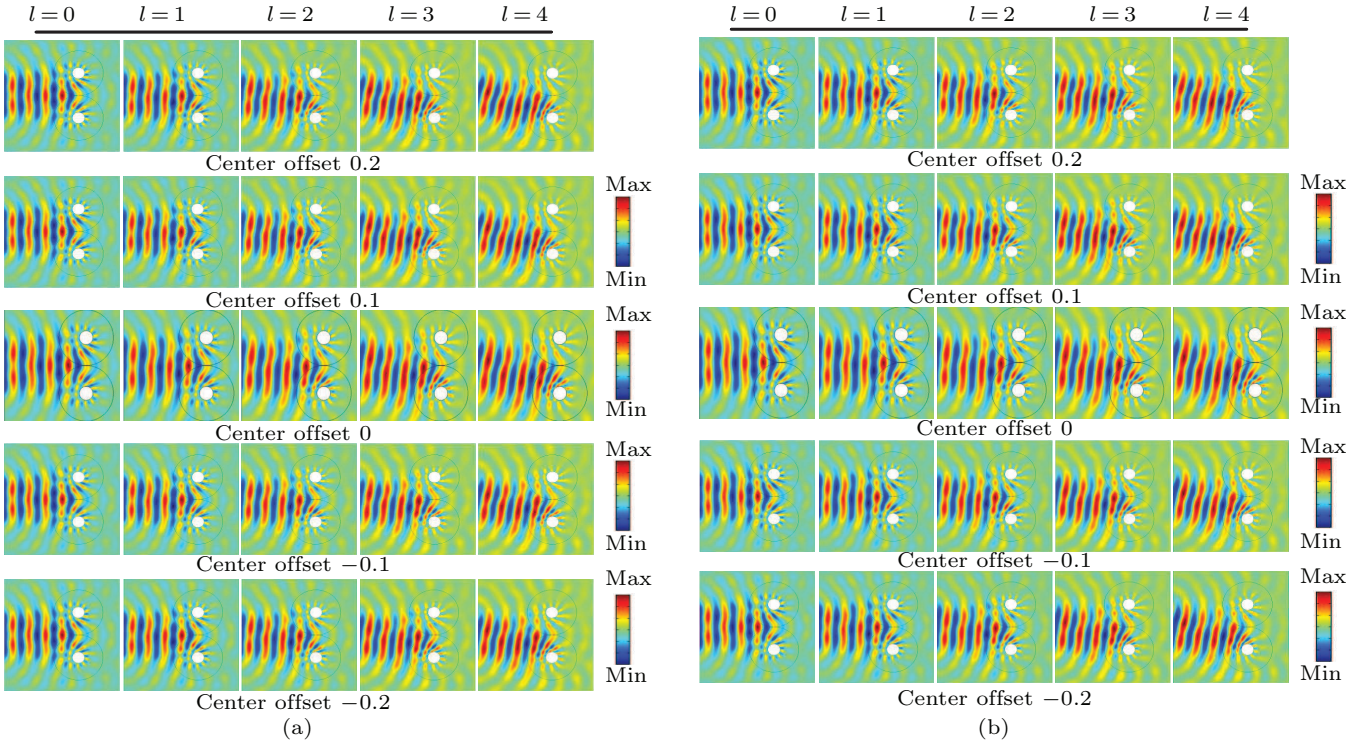


Fig. 11. Wave field distributions in detection layer when input beam center offset along (a) *x* direction and (b) *y* direction.

Table 5. Numerically calculated values of ER and TC of input vortex light wave with different center offsets.

TC	ER (ideal)	ER (nonideal) Beam center offset along *x* direction				ER (nonideal) Beam center offset along *y* direction			
		Center offset −0.2	Center offset −0.1	Center offset 0.1	Center offset 0.2	Center offset −0.2	Center offset −0.1	Center offset 0.1	Center offset 0.2
0	1.02	1.02	1.02	1.02	1.02	1.02	1.02	1.02	1.02
1	1.20	1.19	1.19	1.22	1.23	1.20	1.20	1.20	1.20
2	1.42	1.37	1.39	1.45	1.48	1.41	1.42	1.42	1.41
3	1.68	1.59	1.63	1.74	1.80	1.67	1.68	1.68	1.67
4	1.99	1.86	1.92	2.07	2.16	1.96	1.98	2.00	1.99

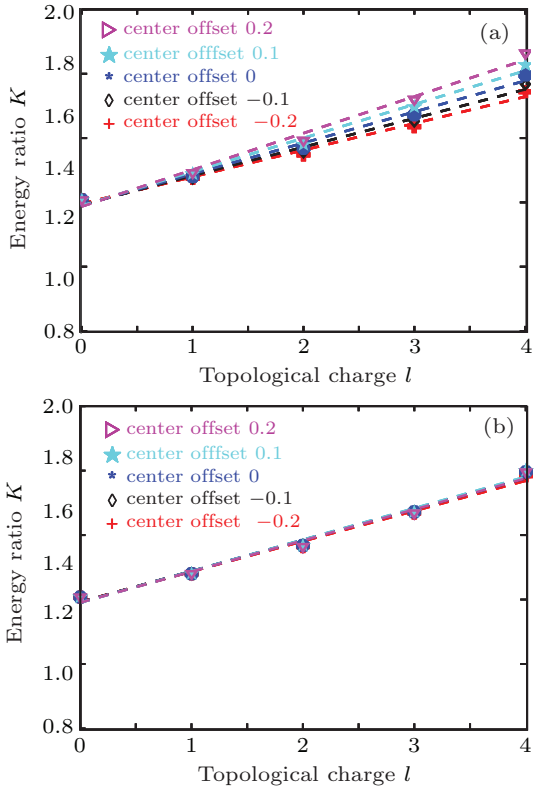


Fig. 12. Numerically calculated relation of ER with TC of input vortex light wave with different offsets along (a) x-axis direction and (b) y-axis direction.

It can be seen from Fig. 12 that when the input beam center has a small position offset along the x-axis or y-axis directions, the linear relation between the ER and the TC is kept and the system can still work well. This can be explained from the derivation in Section 2 that a small position offset will cause a small error of variable β, thus the error of M is also small and in turn the error of energy ratio (K) in Eq. (17) is small.

3.2.3. Nonuniform input wave fields

We suppose that the input wave field is uniform in deriving the linear relation between ER and TC, nevertheless the noise will break this ideal condition, so we need to assess the performance of the system in such cases of nonuniform input wave fields.

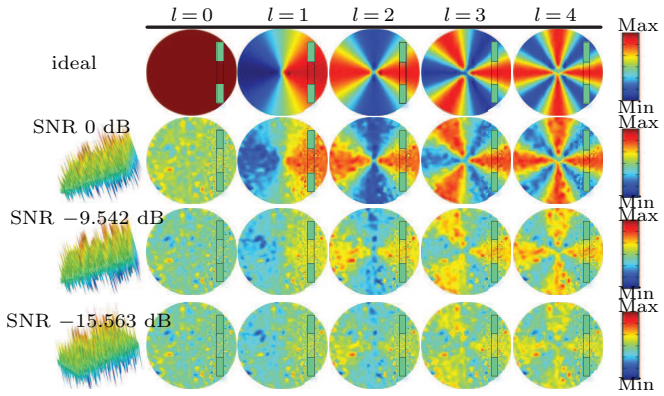


Fig. 13. Input noised fields with different TCs (0–4) at different SNRs.

Here we assume that the nonuniformity is caused by the random noise. Set the signaltonoise ratio (SNR) of the input beam to be 0 dB, −9.542 dB, and −15.563 dB (the corresponding amplitude ratios between signal and noise are 1/1, 1/3, and 1/6) respectively, and compare the relations between the ER and the TC numbers under ideal condition and nonideal condition. The noised input beam fields with different TCs (0–4) are shown in Fig. 13. The wave fields in detection layer are shown in Fig. 14. The numerical results are shown in Table 6 and the corresponding line diagram is shown in Fig. 15.

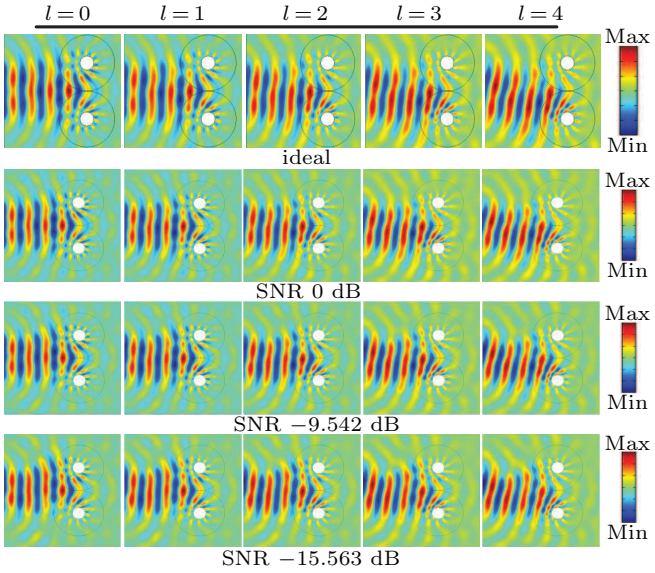


Fig. 14. Wave field distributions in detection layer at at different SNRs.

Table 6. Numerically calculated values of ER and TC in uniform light field and non-uniform light field.

TC	ER (ideal)	ER (nonideal)		
		SNR 0 dB	SNR −9.542 dB	SNR −15.563 dB
0	1.02	1.01	1.08	1.13
1	1.20	1.17	1.11	1.06
2	1.42	1.38	1.32	1.26
3	1.68	1.64	1.57	1. 5
4	1.99	1.95	1.87	1.77

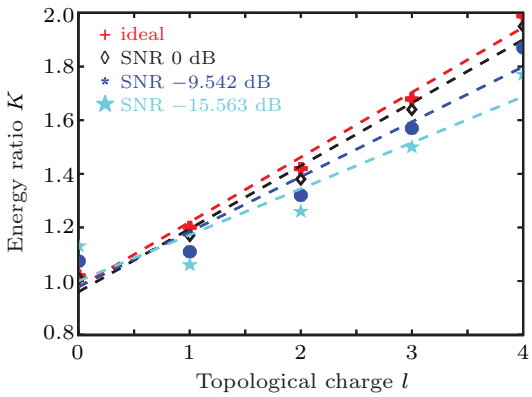


Fig. 15. Numerically calculated relations of ER with TC of uniform light field and non-uniform light field at different SNRs.

It can be seen from Fig. 15 that the system has good anti-noise property and it works well even in 0-dB SNR for random noise. If the noise is very strong, *e.g.*, the SNR lower than −1 dB as adopted in this instance, the linear relation of ER and TC numbers may be distorted and the system may have lower precision.

3.3. Multi-detection layers

There is enough space to set multidetection layers to be in the system, so, it is interesting to find the benefits of such configurations. All the simulations here are carried out at the dimensionless wavelength of 0.4. First we investigate the multiple detection layers stacked in the same orientation. This stacking configuration can be used to detect the input wave fields with ring structure (such as the Gaussian-type vortex beams). The multidetection layers can cover more textures across the ring so they may obtain better detection without moving the detection layer. The single detection layer and three stacking detection layers for a Gaussian-type input vortex beam are checked and the simulation results are shown in Fig. 16.

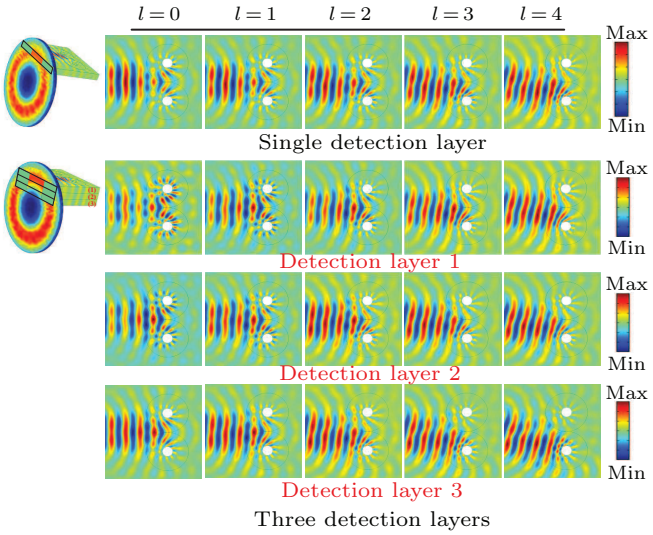


Fig. 16. Wave field distributions in single detection layer and three stacking detection layers.

Table 7. Numerically calculated values of ER and TC of single detection layer and three stacking detection layers.

TC (l)	ER (single layer)	ER (three layers)
–4	1.94	2.05
–3	1.63	1.77
–2	1.35	1.46
–1	1.15	1.20
0	1.00	1.01
1	1.16	1.23
2	1.36	1.50
3	1.64	1.80
4	1.97	2.10

The ER of the stacking detection layer is obtained by averaging those of the three detection layers. The comparison between the ER results of the two devices is shown in Table 7 and the relations of ER with TC are plotted in Fig. 17. The simulation values and theoretical values of ER from the two devices are compared with each other in Table 8.

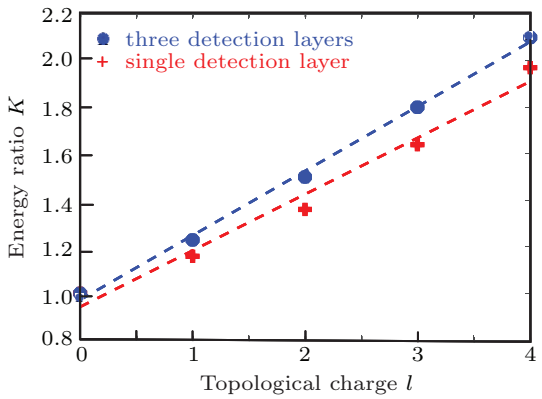


Fig. 17. Numerically calculated relation between ER and TC for single detection layer and three stacking detection layers.

Table 8. Comparison between theoretical and simulation values of ER for single detection layer and three stacking detection layers.

TC (l)	TV	Single detection layer		Three detection layers	
		SV	RE	SV	RE
0	1	1.00	0%	1.01	1%
1	1.3	1.16	11%	1.23	6%
2	1.59	1.36	14%	1.50	6%
3	1.89	1.64	13%	1.80	5%
4	2.19	1.97	10%	2.10	4%

Notes: TV: theoretical value; SV: simulation value; RE: relative error.

These results show that the accuracy of TC measurement of the Gaussian-type vortex beam can be improved by using the stacking multi-detection layers. The stacking system simplifies the process of finding the best input aperture location that a single detection layer system should have for non-uniform (such as ring structured area) input wave field.

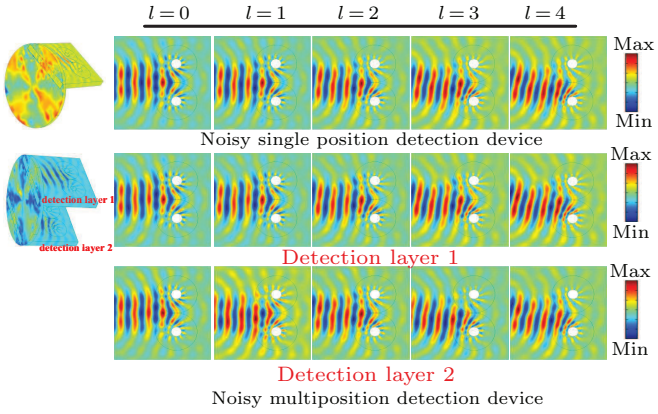


Fig. 18. Wave field distributions on upper surface in noisy single position detection device and noisy multiposition detection device.

Then another configuration of multidetection layers where the layers are azimuthal-equally located is checked. It is expected that the broader detection location may enhance the

stability of the system in random noise environment. Here the distributed multidetection layers are composed of two single detection layers placed 180° apart, and the SNR of the input beam is −9.542 dB. The wave field distribution on the upper surfaces of both the single detection layer and the distributed two detection layers are shown in Fig. 18. The comparison between the ER results of the two systems is shown in Table 9. The relations between ER and TC are plotted in Fig. 19.

Table 9. Numerically calculated values of ER and TC for noisy single position detection devicenoisy multiposition detection device and ideal single detection device.

TC	ER (noisy single detection device)	ER (noisy multiposition detection device)	ER (ideal single detection device)
–4	2.29	2.15	1.96
–3	1.90	1.58	1.66
–2	1.56	1.52	1.38
–1	1.29	1.13	1.16
0	1.08	1.09	1.02
1	1.11	1.23	1.20
2	1.32	1.28	1.42
3	1.57	1.72	1.68
4	1.87	1.80	1.99

The ER of the multiposition system is the average of those of the two layers. In Fig. 19, the fitting line of the multiposition detection system is closer to the ideal one than the single position detection one, which means that the noise effect is lower in the system. However, the number of the detection position should be a tradeoff between the system complexity and effect, which is worth further exploring.

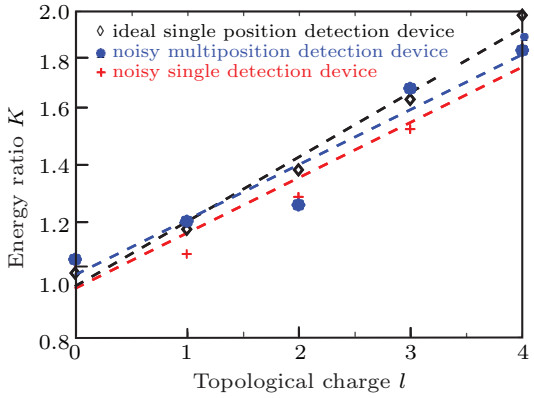


Fig. 19. Numerically calculated relations between ER and TC for noisy single position detection device, noisy multiposition detection device, and ideal single detection device.

4. Discussion and conclusions

A new method of detecting the TC of the vortex beam, called settled measurement, is proposed. In contrast to previously reported methods, which rely on pattern recognition of the manipulated wave field in a region, the proposed method requires only the detection of the wave energy at two fixed points, thus enabling fast and automatic measurement. The key concept of this method is to directly extract the plane wave from the vortex beam by using a simple configuration, after which the plane wave is guided and split into a system of twin OEAs. A different TC will lead to a different ER in the twin OEAs; in turn, the TC can be obtained by quantitatively detecting the two sensors inside the twin OEAs. It should be noted that the OEA is not inevitably based on the proposed spiral-to-plane wave extraction idea. Although the energy allocation can still be distinguished in the detection line even without the OEA, the cost of a sensor array or vast sensors might lose the conciseness as that of the proposed device. The detection needs some prior information about such as wavelength, device size, *etc*., however it is not a challenge for practical application. The simulation results verify the effectiveness of the proposed device. In addition, the robustness of the proposed system working in a non-ideal condition is investigated, including the incidence direction deviation, input beam center offset, and nonuniform input wave field. Generally speaking, the tiny scale of such system errors will not remarkably influence the device, and if the errors are considerable large, the system may need calibrating correspondingly in advance. Although this method is not perfect, it has important potential applications in the field of communication or industrial because of its simple and compact structure.

The fractional order vortex structure is distorted, and if the two fractional TCs are too close to each other, the difference between adjacent angles of conversion inclination beam is not obvious enough, which may lead to inaccurate measurement accuracy so the current method may be not applicable in such cases.

It is also worth noting that the OEAs in the detection layer are just two-dimensional (2D), it is possible to manufacture the devices through using various technologies.[55,61–63] Moreover, with the current development of three-dimensional (3D) printing technology,[64–68] the 2D device with high precision of refractive index can be fabricated, implying that the method possesses many potential practical applications. Although at present there exists no experiment on the verification for the proposed method, the idea itself is instructive and the sufficient discussion may lay a good foundation for future experiments, so the work is meaningful, we think.

References

[1] Allen L, Beijersbergen M W, Spreeuw R J C and Woerdman J P 1992 *Phys. Rev. A* **45** 8185
[2] Dholakia K and Čižmár T 2011 *Nat. Photon.* **5** 335
[3] Grier D G 2003 *Nature* **424** 810
[4] Karimipour V, Bahraminasab A and Bagherinezhad S 2002 *Phys. Rev. A* **65** 042320
[5] Vaziri A, Pan J W, Jennewein T, Weihs G and Zeilinger A 2003 *Phys. Rev. Lett.* **91** 227902
[6] Aiello A, Oemrawsingh S S R, Eliel E R and Woerdman J P 2005 *Phys. Rev. A* **72** 052114
[7] Djordjevic I B 2011 *Opt. Express* **19** 14277
[8] Wang J, Yang J-Y, Fazal I M, Ahmed N, Yan Y, Huang H, Ren Y, Yue Y, Dolinar S, Tur M and Willner A E 2012 *Nat. Photon.* **6** 488

[9] Ren Y, Wang Z, Xie G, Li L, Cao Y, Liu C, Liao P, Yan Y, Ahmed N, Zhao Z, Willner A, Ashrafi N, Ashrafi S, Linquist R D, Bock R, Tur M, Molisch A F and Willner A E 2015 *Opt. Lett.* **40** 4210

[10] Li L and Li F 2013 *Phys. Rev. E* **88** 033205

[11] Barbieri C, Tamburini F, Anzolin G, Bianchini A, Mari E, Sponselli A, Umbriaco G, Prasciolu M, Romanato F and Villoresi P 2009 *Earth Moon Planet* **105** 283

[12] Lavery M P J, Speirits F C, Barnett S M and Padgett M J 2013 *Science* **341** 537

[13] Hakobyan D and Brasselet E 2015 *Opt. Express* **23** 31230

[14] Lavery M P J, Barnett S M, Speirits F C and Padgett M J 2014 *Optica* **1** 1

[15] Li X, Tai Y, Lv F and Nie Z 2015 *Opt. Commun.* **334** 235

[16] Ma H, Li X, Tai Y, Li H, Wang J, Tang M, Wang Y, Tang J and Nie Z 2017 *Opt. Lett.* **42** 135

[17] Liu Y and Pu J 2011 *Opt. Commun.* **284** 2424

[18] Bahl M and Senthilkumaran P 2015 *Phys. Rev. A* **92** 013831

[19] Brandão P A and Cavalcanti S B 2016 *Phys. Lett. A* **380** 4013

[20] Guo C S, Lu L L and Wang H T 2009 *Opt. Lett.* **34** 3686

[21] Jian-Long L 2010 *Chin. Phys. B* **19** 104001

[22] Ji Z Y and Zhou G Q 2017 *Chin. Phys. B* **26** 094202

[23] Ghai D P, Senthilkumaran P and Sirohi R S 2009 *Opt. Lasers Eng.* **47** 123

[24] Sztul H I and Alfano R R 2006 *Opt. Lett.* **31** 999

[25] Liu R, Long J, Wang F, Wang Y, Zhang P, Gao H and Li F 2013 *J. Opt* **15** 125712

[26] Fu D, Chen D, Liu R, Wang Y, Gao H, Li F and Zhang P 2015 *Opt. Lett.* **40** 788

[27] Zhu J, Zhang P, Chen D, Liu R, Zhou Y, Wang J, Gao H and Li F 2018 *Appl. Opt.* **57** B39

[28] Guo C S, Yue S J and Wei G X 2009 *Appl. Phys. Lett.* **94** 231104

[29] Zhao Q, Dong M, Bai Y and Yang Y 2020 *Photon. Res.* **8** 745

[30] Narag J P C and Hermosa N 2019 *Phys. Rev. Appl.* **11** 054025

[31] Dai K, Gao C, Zhong L, Na Q and Wang Q 2015 *Opt. Lett.* **40** 562

[32] Saitoh K, Hasegawa Y, Hirakawa K, Tanaka N and Uchida M 2013 *Phys. Rev. Lett.* **111** 074801

[33] Zheng S and Wang J 2017 *Sci. Rep.* **7** 40781

[34] Guzzinati G, Clark L, Béché A and Verbeeck J 2014 *Phys. Rev. A* **89** 025803

[35] Gao C, Qi X, Liu Y, Xin J and Wang L 2011 *Opt. Commun.* **284** 48

[36] Leach J, Courtial J, Skeldon K, Barnett S M, Franke-Arnold S and Padgett M J 2004 *Phys. Rev. Lett.* **92** 013601

[37] Leach J, Padgett M J, Barnett S M, Franke-Arnold S and Courtial J 2002 *Phys. Rev. Lett.* **88** 257901

[38] Pors J B, Aiello A, Oemrawsingh S S R, van Exter M P, Eliel E R and Woerdman J P 2008 *Phys. Rev. A* **77** 033845

[39] Berkhout G C G, Lavery M P J, Padgett M J and Beijersbergen M W 2011 *Opt. Lett.* **36** 1863

[40] Oemrawsingh S S R, Eliel E R, Nienhuis G and Woerdman J P 2004 *J. Opt. Soc. Am. A* **21** 2089

[41] Guo Z Y, Qu S L, Sun Z H and Liu S T 2008 *Chin. Phys. B* **17** 4199

[42] Harris M, Hill C A, Tapster P R and Vaughan J M 1994 *Phys. Rev. A* **49** 3119

[43] Berkhout G C G, Lavery M P J, Courtial J, Beijersbergen M W and Padgett M J 2010 *Phys. Rev. Lett.* **105** 153601

[44] Lavery M P J, Berkhout G C G, Courtial J and Padgett M J 2011 *J. Opt* **13** 064006

[45] Wen Y, Chremmos I, Chen Y, Zhu J, Zhang Y and Yu S 2018 *Phys. Rev. Lett.* **120** 193904

[46] Prabhakar S, Kumar A, Banerji J and Singh R P 2011 *Opt. Lett.* **36** 4398

[47] Zhang X, Xia T, Cheng S and Tao S 2019 *Opt. Commun.* **431** 238

[48] Han Y and Zhao G 2011 *Opt. Lett.* **36** 2017

[49] Vaity P, Banerji J and Singh R P 2013 *Phys. Lett. A* **377** 1154

[50] Liu A P, Xiong X, Ren X F, Cai Y J, Rui G H, Zhan Q W, Guo G C and Guo G P 2013 *Sci. Rep.* **3** 2402

[51] Zhang Z, Dong F, Qian K, Zhang Q, Chu W, Zhang Y, Ma X and Wu X 2015 *Opt. Express* **23** 20521

[52] Genevet P, Lin J, Kats M A and Capasso F 2012 *Nat. Commun.* **3** 1278

[53] Rui G, Gu B, Cui Y and Zhan Q 2016 *Sci. Rep.* **6** 28262

[54] Abramowitz M and Stegun I A 1948 *Handbook of mathematical functions with formulas, graphys, and mathematical tables* (US Government Printing Office)

[55] Narimanov E E and Kildishev A V 2009 *Appl. Phys. Lett.* **95** 041106

[56] Chang Z and Hu G 2012 *Appl. Phys. Lett.* **101** 054102

[57] Goodman J W 1996 *Introduction to Fourier Optics*, 3rd edn. (McGraw-Hill)

[58] Ozaktas H M and Mendlovic D 1995 *J. Opt. Soc. Am. A* **12** 743

[59] Yang X and Hu J 2018 *Opt. Express* **26** 27528

[60] Eberhard Z 2004 *Oxford users' guide to mathematics* (Oxford University Press)

[61] Cheng Q, Cui T J, Jiang W X and Cai B G 2010 *New J. Phys.* **12** 063006

[62] Wang H W and Chen L W 2011 *J. Appl. Phys.* **109** 103104

[63] Lu W, Jin J, Lin Z and Chen H 2010 *J. Appl. Phys.* **108** 064517

[64] Jonušauskas L, Gailevičius D, Rekštytė S, Baldacchini T, Juodkazis S and Malinauskas M 2018 *Opt. Express* **27** 15205

[65] Bandyopadhyay A and Heer B 2018 *Materials Science and Engineering: R: Reports* **129** 1

[66] Tian X, Yin M and Li D 2016 *RPJ* **22** 251

[67] Jiang W X, Ge S, Han T, Zhang S, Mehmood M Q, Qiu C W and Cui T J 2016 *Adv. Sci.* **3** 1600022

[68] Yin L, Doyhamboure–Fouquet J, Tian X and Li D 2018 *Composites Part B: Engineering* **132** 178